The Astrophysical Journal Supplement Series, 247:71 (15pp), 2020 April https://doi.org/10.3847/1538-4365/ab799e

Deciphering the Large-scale Environment of Radio Galaxies in the Local Universe. II. A Statistical Analysis of Environmental Properties

F. Massaro[1,2,3,4], A. Capetti[2], A. Paggi[1,2,3], R. D. Baldi[5], A. Tramacere[6], I. Pillitteri[7], R. Campana[8], A. Jimenez-Gallardo[1,2], and V. Missaglia[9]
[1] Dipartimento di Fisica, Università degli Studi di Torino, via Pietro Giuria 1, I-10125 Torino, Italy
[2] INAF-Osservatorio Astrofisico di Torino, via Osservatorio 20, I-10025 Pino Torinese, Italy
[3] Istituto Nazionale di Fisica Nucleare, Sezione di Torino, I-10125 Torino, Italy
[4] Consorzio Interuniversitario per la Fisica Spaziale, via Pietro Giuria 1, I-10125 Torino, Italy
[5] Department of Physics and Astronomy, University of Southampton, Highfield, SO17 1BJ, UK
[6] University of Geneva, Chemin d'Ecogia 16, Versoix, CH-1290, Switzerland
[7] INAF-Osservatorio Astronomico di Palermo G.S. Vaiana, Piazza del Parlamento 1, I-90134, Italy
[8] INAF/OAS, via Piero Gobetti 101, I-40129, Bologna, Italy
[9] Harvard—Smithsonian Astrophysical Observatory, 60 Garden Street, 02138, Cambridge (MA), USA
Received 2019 March 1; revised 2020 February 18; accepted 2020 February 20; published 2020 April 14

Abstract

In our previous analysis we investigated the large-scale environment of two samples of radio galaxies (RGs) in the local universe (i.e., with redshifts $z_{\rm src} \leqslant 0.15$), classified as FR I and FR II on the basis of their radio morphology. The analysis was carried out using (i) extremely homogeneous catalogs and (ii) a new method, known as cosmological overdensity, to investigate their large-scale environments. We concluded that, independently of the shape of their radio extended structure, RGs inhabit galaxy-rich large-scale environments with similar characteristics and richness. In the present work, we first highlight additional advantages of our procedure, which does not suffer cosmological biases and/or artifacts, and then we carry out an additional statistical test to strengthen our previous results. We also investigate properties of RG environments using those of the cosmological neighbors. We find that large-scale environments of both FR Is and FR IIs are remarkably similar and independent of the properties of central RG. Finally, we highlight the importance of comparing radio sources in the same redshift bins to obtain a complete overview of their large-scale environments.

Unified Astronomy Thesaurus concepts: Relativistic jets (1390); Astrostatistics (1882); Active galaxies (17); Radio galaxies (1343); Galaxy clusters (584)

Supporting material: machine-readable table

1. Introduction

In the last few decades, extensive multifrequency investigations, combined with different statistical procedures, have shown that radio galaxies (RGs) preferentially inhabit galaxy-rich large-scale environments (see, e.g., Prestage & Peacock 1988; Hill & Lilly 1991; Zirbel 1997; Worrall & Birkinshaw 2000; Belsole et al. 2007; Tasse et al. 2008), making them ideal laboratories to investigate formation and evolution of cosmological structures (see also Best 2004; Gendre et al. 2013; Ineson et al. 2013, 2015). Most of these studies compare different classes of RGs, distinguishing between FR I (i.e., edge-darkened) and FR II (i.e., edge-brightened) classes (Fanaroff & Riley 1974) or between low excitation and high excitation RGs (LERGs and HERGS, respectively; see, e.g., Hine & Longair 1979; Laing et al. 1994).

The most efficient approaches that allow us to get a complete overview of both galaxies and intergalactic medium (IGM) are certainly those based on or combined with X-ray observations (see, e.g., Hardcastle & Worrall 2000; Ineson et al. 2013, 2015). Although in the last few decades, thanks to *XMM-Newton* and *Chandra* campaigns, X-ray archives have been enriched by RG observations (see, e.g., Evans et al. 2006; Croston et al. 2008; Massaro et al. 2012, 2015, 2018; Mingo et al. 2014, 2017; Stuardi et al. 2018, for recent results), the largest fraction of the analyses carried out to date on their large-scale environments are preferentially based on optical and infrared surveys (see, e.g., Ching et al. 2017; Miraghaei & Best 2017; Massaro et al. 2019). This is mainly due to difficulties on performing deep and, at the same time, wide-area X-ray surveys, that would allow us to avoid biases introduced by a scarce sampling of RG populations. Results achieved to date are not always in agreement.

We recently proposed a different approach based on the selection of extremely homogenous data sets, restricted to the local universe (i.e., source redshifts $z_{\rm src} \leqslant 0.15$), to shed light on RG large-scale environments (Massaro et al. 2019, hereinafter M19).

We first created two homogeneous catalogs of FR I and FR II RGs (hereinafter FRICAT and FRIICAT, respectively; Capetti et al. 2017a, 2017b) at a high level of completeness (i.e., ∼95%) based on uniform radio images made available thanks to the Faint Images of the Radio Sky at Twenty cm radio survey (White et al. 1997; Helfand et al. 2015), which has almost the same footprint as the Sloan Digital Sky Survey (see, e.g., Ahn et al. 2012) and is also completely covered by the NRAO VLA Sky Survey (Condon et al. 1998)—and mid-infrared images, available thanks to the observations of the *Wide-field Infrared Survey Explorer* (i.e., *WISE*; Wright et al. 2010). Then our investigation compared the efficiency of several clustering algorithms, including a new procedure, known as cosmological overdensity, based on the so-called cosmological neighbors (see the following sections for more details), opportunely developed to avoid cosmological biases and artifacts.

We mainly concluded that RGs, independently of their radio (FR I versus FR II) or optical classification (LERG versus

HERG), tend to inhabit galaxy-rich large-scale environments with similar richness (M19). However, the limited number of HERGs present in our FRIICAT prevented us from drawing firm statistical conclusions when comparing LERG and HERG populations; thus, the statement based on the optical classification has to be treated with caution, as it requires a deeper analysis. Finally, we highlighted the importance of comparing radio sources in the same redshift bins to obtain a complete overview of their large-scale environments. It is worth highlighting that searching for galaxy clusters and groups using spectroscopic redshifts is a method that has already been used in the past (see, e.g., Danese et al. 1980; Huchra & Geller 1982; Girardi et al. 1993; Fadda et al. 1996).

Here we first present additional evidence of cosmological biases and artifacts that could affect analyses of the large-scale environments highlighting the advantages of the cosmological overdensity method. Then we perform an additional statistical test to obtain a direct comparison between the FR I and the FR II populations. On the basis of the distribution of optical sources surrounding RGs, we also present a new set of parameters to (i) characterize and (ii) compare their large-scale environments.

The paper is organized as follows. In Section 2 we describe the samples selected to carry out our analysis while in Section 3 we provide a brief description of the cosmological overdensity procedure. Additional evidence of cosmological biases and artifacts that could arise in similar analyses is given in Section 4. Then in Section 5 we present a new statistical test that strengthens the evidence that FR Is and FR IIs inhabit similar galaxy-rich large-scale environments, while Section 6 is devoted to the description of several ambient parameters obtainable from the distribution of cosmological neighbors. Section 7 is then dedicated on future developments achievable with dedicated X-ray observations. Finally, a summary and our conclusions are given in Section 8 with tables and additional figures reported in the Appendix.

As in M19, we adopt cgs units for numerical results and we assume a flat cosmology with $H_0 = 69.6\,\mathrm{km\,s^{-1}\ Mpc^{-1}}$, $\Omega_M = 0.286$, and $\Omega_\Lambda = 0.714$ (Bennett et al. 2014), unless otherwise stated. Thus, according to these cosmological parameters, $1''$ corresponds to 0.408 kpc at $z_{src} = 0.02$ and to 2.634 kpc at $z_{src} = 0.15$.

2. Sample Selection

We selected two RG catalogs to carry out our analysis starting from the radio-loud sample of Best & Heckman (2012).

The first catalog is the combination of FRICAT and sFRICAT both described in Capetti et al. (2017a). The FRICAT sources, chosen on the basis of their FR I radio morphology, are selected to have a radio structure beyond a distance of 30 kpc, measured from the optical position of the host galaxy, with the only exceptions of the 14 sFRICAT objects with radio extended emission having the same morphology but extending between 10 and 30 kpc but limited to $z_{src} = 0.05$ (see Capetti et al. 2017a for details). This combination of these two samples includes RGs at redshift $z_{src} \leqslant 0.15$, all hosted in red early-type galaxies and spectroscopically classified low excitation radio galaxies (LERGs) for a total of 209 radio sources.

The second sample is the FRIICAT (Capetti et al. 2017b), composed of 105 edge-brightened radio sources (FR II type) within the same redshift range of the previous catalog. About ∼90% of the FR IIs listed in the FRIICAT are spectroscopically classified as LERGs, being hosted red early-type galaxies as occurs for FR Is. The remaining ∼10% of the FRIICAT shows indeed optical spectra typical of high excitation radio galaxies (HERGs) and host galaxies bluer in the optical band and redder in the infrared than FR II LERGs.

Thanks to their selection criteria both RG catalogs are not contaminated by compact radio objects, as compact steep spectrum sources and FR 0s (Baldi et al. 2015, 2018), which show a different cosmological evolution, with respect to FR Is and FR IIs and could potentially lie in different environments.

The selected RG catalogs include only sources lying in the central footprint of the SDSS, because it is the same sky area covered by the main catalog of groups and clusters of galaxies adopted in our analysis: the one created by Tempel et al. (2012, hereinafter T12). The T12 catalog has the largest number of cluster/group detections with spectroscopic redshifts z_{cl} in the range between 0.009 and 0.20 and peaking around 0.08. This catalog of groups and clusters is based on a modified version of the Friends-of-Friends algorithm (Huchra & Geller 1982; Tago et al. 2010) and its richness is indicated as N_{gal}.

3. Cosmological Overdensity

Our analysis on the large-scale environment of RGs is based on the definition of two types of optical sources lying within 2 Mpc. These are the (i) cosmological neighbors and the (ii) candidate elliptical galaxies whose definition is reported below, for the sake of completeness.

1. Cosmological neighbors: all optical sources lying within the 2 Mpc radius computed at z_{src} of the central radio galaxy with all the SDSS magnitude flags indicating a galaxy-type object (i.e., $uc = rc = gc = ic = zc = 3$), and having a spectroscopic redshift z with $\Delta z = |z_{src} - z| \leqslant 0.005$, corresponding to the maximum velocity dispersion in groups and clusters of galaxies (see, e.g., Moore et al. 1993; Eke 2004; Berlind et al. 2006).

We indicate the number of cosmological neighbors, N_{cn}^{500}, N_{cn}^{1000}, and N_{cn}^{2000}, lying within 500 kpc, 1 Mpc and 2 Mpc distance from the central radio galaxy, respectively, that provide an estimate of the environmental richness.

2. Candidate elliptical galaxies: all SDSS sources, lying within the 2 Mpc distance from the central RG at z_{src} and with $u - r$ and $g - z$ optical colors consistent with those of a sample of elliptical galaxies, chosen out of the galaxy zoo project (Lintott et al. 2008), at the same redshift and within the 90% level of confidence evaluated using the Kernel Density Estimator (Richards et al. 2004; D'Abrusco et al. 2009; Massaro et al. 2011, 2013).

We selected elliptical-type galaxies because their density in galaxy groups or clusters is larger than that of spirals (see, e.g., Biviano 2000).

Source selected as candidate elliptical galaxies do not necessarily have spectroscopic z_{src} estimates.

Candidate elliptical galaxies were mainly used in the previous analysis with the following two aims. First, they allow us to check galaxy-rich environments also when the number of cosmological neighbors is limited, since we were able to test the presence of the "red sequence" (i.e., the well-known relation between colors and magnitude for galaxies that are members of groups and/or clusters Visvanathan & Sandage 1977; Gladders et al. 1998; Gladders & Yee 2000) with two different color–magnitude diagrams (see M19 for more details). Then the distance between the fifth candidate elliptical galaxy and the central RG was used to compute the Σ_5

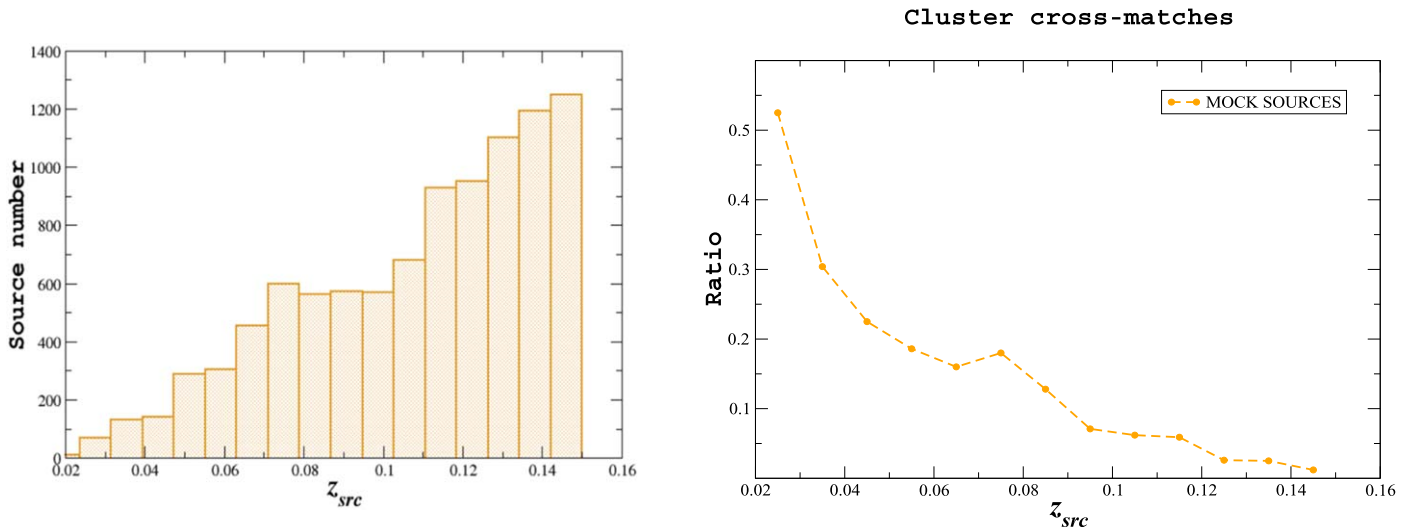

Figure 1. (Left panel) The $z_{\rm src}$ distribution of 9800 random positions (i.e., mock sources) chosen in the SDSS footprint, lacking a radio counterpart within 5″. (Right panel) The ratio between the number of mock sources having a group or a cluster of galaxies with richness $N_{\rm gal} > 4$ from the T12 catalog and with having $\Delta z = |z_{\rm src} - z_{\rm cl}| \leqslant 0.005$, and the total number of mock sources in a bin of $z_{\rm src}$ of size 0.01. This confirms our previous results based on a mock catalog of 5000 sources (Massaro et al. 2019) that it is easier to find a positive cross-match at low $z_{\rm src}$.

parameter as an estimator of the richness (see, e.g., Haas et al. 2012; Sabater et al. 2013; Worpel et al. 2013).

Based on our criterion, a cosmological overdensity occurs when the number of cosmological neighbors counted within 500 kpc is higher than the 95% quantile of the N_{cn}^{500} distribution measured for a sample of mock sources located in random positions of the sky. This $N_{\rm cn}^{500}$ threshold has been chosen in bin of $z_{\rm src}$ of size 0.01 to compare sources at same redshifts thus to avoid cosmological biases and artifacts. At redshifts above 0.1 we imposed to have at least two cosmological neighbors within 1 Mpc in addition to the previous criterion on $N_{\rm cn}^{500}$. Additional and more specific details about this procedure can be found in M19.

4. Cosmological Biases and Artifacts

Here we describe several cosmological biases and artifacts encountered while carrying out our investigation to highlight advantages of using, whenever possible, the method of cosmological overdensity.

4.1. Biases in the Catalog Cross-matches

Cross-matches with catalogs of groups and clusters of galaxies show a clear $z_{\rm src}$ dependence. As shown in Figure 1, we built a sample of 9800 random positions in the SDSS footprint and cross-matched it with the T12 catalog. The redshift distribution of mock sources rises up to $z_{\rm src} = 0.15$ as those of FRICAT and FRIICAT.

The fraction of mock sources per redshift bin of size 0.01 having a positive cross-match with a group or a cluster of galaxies within 2 Mpc, computing its $z_{\rm src}$, and having $\Delta z = |z_{\rm src} - z_{\rm cl}| \leqslant 0.005$ and $N_{\rm gal} > 4$, significantly decreases while $z_{\rm src}$ increases. This indicates that we could expect a higher chance of finding a low-redshift RG associated with a group or a galaxy cluster than a high-redshift one. Thus we chose the thresholds on the number of cosmological neighbors in the cosmological overdensity as a function of $z_{\rm src}$.

A second problem arises when using catalog cross-matches regarding the richness estimated. In Figure 2 we show the difference ΔN between the number of cosmological neighbors, $N_{\rm cn}^{2000}$ lying within 2 Mpc distance from the central RG and $N_{\rm gal}$

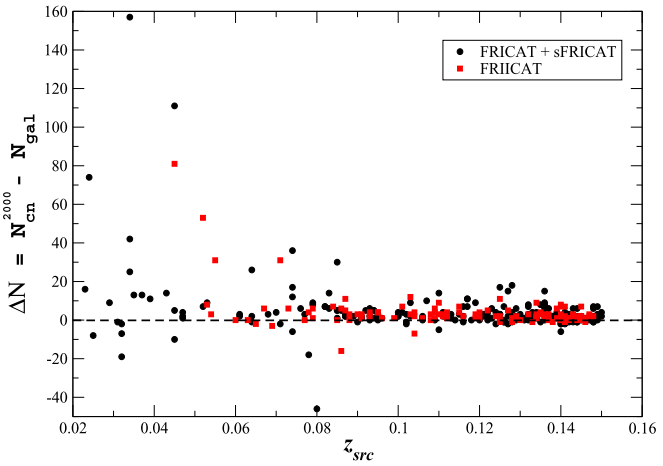

Figure 2. Difference, ΔN, between the number of cosmological neighbors, $N_{\rm cn}^{2000}$ lying within 2 Mpc distance from the central RG and $N_{\rm gal}$ being the richness estimated in the T12 cluster catalog. Black circles mark radio sources in the FRICAT, including those of the sFRICAT, while red squares correspond to the FR IIs.

from the T12 group/cluster catalog. It is quite evident that the $N_{\rm gal}$ parameter underestimates the group/cluster richness. There are only a few cases where $N_{\rm cn}^{2000}$ provides a lower estimate of the group/cluster richness. However, these cases could be also due to an incorrect run of the algorithm of the T12 catalog since we did not detect sources lying at similar redshift of the central RG and not even candidate elliptical galaxies for most of them. It is worth noting that the richness estimated in cluster catalogs is generally decreasing with redshift, as, for example, occurs for $N_{\rm gal}$ in the T12; thus, we expect to find less galaxy-rich environments as $z_{\rm src}$ increases.

An additional advantage of the method based on the cosmological overdensity with respect to the cluster catalog cross-matches includes the estimate of the position of the central RG with respect to cluster center both in angular separation and redshift. In Figure 3 we show the projected distance, $d_{\rm proj}$, measured between the position of the RG in the

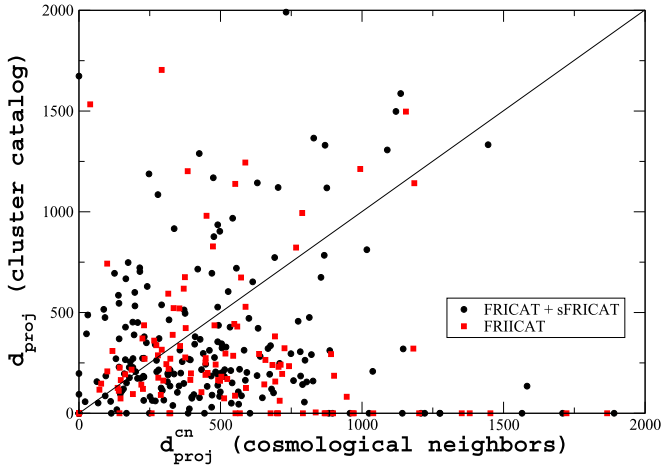

Figure 3. On the x-axis we report the projected distance, $d_{\rm proj}$, measured between the position of the RG in the center of the field examined and the centroid of the spatial distribution of cosmological neighbors within 2 Mpc, while on the y-axis the projected distance is computed using the location of the closest group/cluster positionally associated with the T12 catalog. As in Figure 2 black circles mark radio sources in the FRICAT, including those of the sFRICAT, while red squares correspond to the FR IIs.

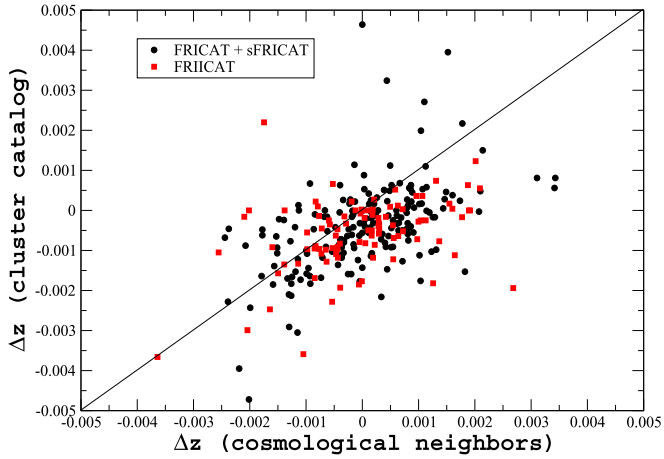

Figure 4. Redshift difference, $\Delta\, z$, between the central RG $z_{\rm src}$ and the average value of the cosmological neighbors lying within 2 Mpc (x-axis) in comparison with that estimated using the spectroscopic redshift of the closest cluster associated with the T12 catalog (y-axis). Sources belonging to both FRICAT and sFRICAT are shown as black circles while FR IIs are shown as red squares.

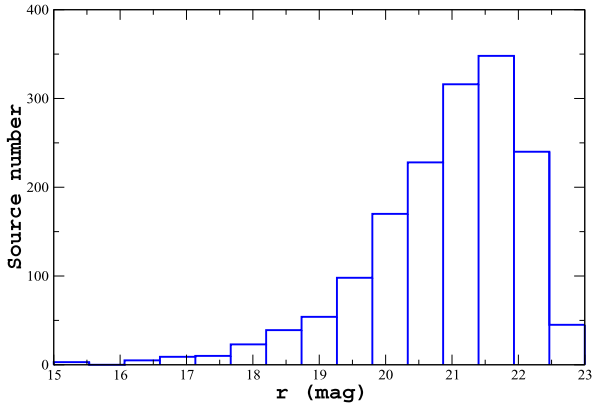

Figure 5. Distribution of the R band apparent magnitude r of all SDSS sources classified as galaxies (i.e., $uc = rc = gc = ic = zc = 3$) in the 2 Mpc field of the FR I SDSSJ073505.25+415827.5. It is evident how the number of sources increases drastically when r increases up to the completeness level of the SDSS.

center of the field examined and (i) the centroid of the spatial distribution of cosmological neighbors within 2 Mpc (x-axis) or (ii) that of the group/cluster reported in the T12 catalog (y-axis). The majority of sources have values below bisector, indicating that $d_{\rm proj}$ estimated via cosmological neighbors tend to be smaller than those evaluated with the T12 catalog.

Finally, in Figure 4 we show the redshift difference, $\Delta\, z$, between the central RG $z_{\rm src}$ and (i) the average value of the cosmological neighbors lying within 2 Mpc (x-axis) and (ii) the redshift of the closest cluster associated using the T12 catalog (y-axis). Once again the largest fraction of RG in both FRICAT and FRIICAT lies below the bisector, highlighting that cosmological neighbors provide a better sampling of the RG large-scale environment. Assuming that all RGs belong to a galaxy group/cluster, thanks to the distribution of cosmological neighbors we can achieve a better estimate of its redshift: $z_{\rm cl}$.

4.2. Cosmological Dependences of Noise

Selecting candidate elliptical galaxies on the basis of their spectroscopic redshift, whenever possible, is more precise than, for example, performing a simple magnitude cut as to estimate the Abell environmental richness. Counting overdensity of optical sources within a certain distance in kiloparsecs and with apparent magnitude $m \leqslant m_{\rm src} + 2$, with $m_{\rm src}$ being the apparent magnitude of the central radio source (see, e.g., Hill & Lilly 1991), introduces a significant amount of noise due to background and foreground objects being counted. This occurs because the number of optical galaxies increases significantly with the magnitude as shown, for example, in Figure 5 for the R band apparent magnitude of galaxy-type objects (i.e., $uc = rc = gc = ic = zc = 3$) in the 2 Mpc field of the FR I SDSSJ073505.25+415827.5. Thus comparing overdensity of optical sources around RG lying at different $z_{\rm src}$ when they have the same absolute magnitudes, or simply different apparent magnitudes, implies comparing sources with different signal-to-noise ratios. This makes the comparison between source populations with different redshift distributions, different apparent magnitude distributions, and/or similar intrinsic luminosity/absolute magnitudes, such as FR Is and FR IIs, challenging. This effect could be mitigated by counting number sources per unit of area, since, at larger redshifts, areas of the same physical size appear smaller and thus contain fewer background/foreground sources (i.e., less noise). On the other hand, this does not help since it introduces a cosmological dependence on the noise.

In addition, sources selected to be galaxies above a certain threshold of apparent magnitude do not necessarily belong to the same group or cluster of galaxies. In Figure 6, we show the ratio between the total number of cosmological neighbors and that of optical sources with spectroscopic redshifts both selected to have $m \leqslant m_{\rm src} + 2$ in the R band, similar to the definition of Abell classes (see, e.g., Abell et al. 1989), within 2 Mpc distance from all FR Is listed in the FRICAT. Only 30%–40% are generally lying at similar redshifts being so classifiable as cosmological neighbors, while others are simply background and foreground sources (i.e., noise), with very different redshifts, and thus are erroneously counted. Noise-related effects related to the source selection with certain

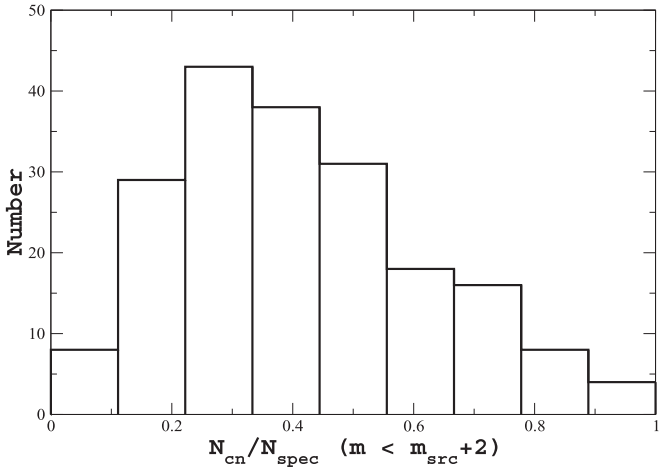

Figure 6. Distribution of the ratio between the total number of cosmological neighbors and that of optical sources with spectroscopic redshifts both selected to have $m \leqslant m_{\rm src} + 2$, in the R band, in the field of all FR Is lying within 2 Mpc form the central RG. This distribution shows how selecting sources only on the basis of their SDSS magnitude introduces more noise since, out of the sources with spectroscopic redshift, only a tiny fraction, on average, appear to be gravitationally bounded with the central RG.

apparent magnitude can be partially mitigated by using photometric redshift estimates, as those provided in the SDSS, and counting sources on the basis of their absolute magnitudes and $V-R$ color (see, e.g., Blanton et al. 2000, 2001; Wing & Blanton 2011, and references therein), but not fully avoided. On the other hand, as shown in M19, the cosmological overdensity method does not suffer this noise effect since the threshold to indicate sources in a galaxy-rich large-scale environment is chosen as a function of redshift and because we compare RGs in the same redshift bin.

4.3. Redshift Evolution of the Cosmological Overdensity

Here we show the underlying reason for adopting an "adaptive" procedure, as the cosmological overdensity method, with a threshold on the number of cosmological neighbors changing with redshift $z_{\rm src}$.

In Figure 7 we show the 2 Mpc field around the FR I SDSS J160722.95+135316.4 at $z_{\rm src} = 0.034$, where red circles mark the locations of cosmological neighbors and dashed lines the distances of 1 Mpc and 2 Mpc, respectively. We computed the absolute magnitude in the R band of all cosmological neighbors and then, maintaining their intrinsic power, we rescaled them at larger distances, namely at redshifts 0.05, 0.10, and 0.15. We also recomputed the radii of the circles of 500 kpc, 1 Mpc, and 2 Mpc at each redshift.

In each plot of Figure 7 we only reported those cosmological neighbors with rescaled apparent magnitudes, m_r, brighter than 17.8, corresponding to the SDSS criterion, to select targets for spectroscopic observations. For the case of SDSS J160722.95 +135316.4, the number of cosmological neighbors within 500 kpc (i.e., $N_{\rm cn}^{500}$) decreases from 10 at $z_{\rm src} = 0.034$, to 3, 2 at $z_{\rm src} = 0.05$, 0.10 and none at $z_{\rm src} = 0.15$, respectively, while $N_{\rm cn}^{2000}$ is actually 47 at 0.034 and 20, 4, 1 at $z_{\rm src} = 0.05$, 0.10, 0.15, respectively.

This suggests that the threshold chosen to indicate a galaxy-rich large-scale environment must be redshift dependent as we defined in our previous analysis on the basis of the Monte Carlo simulations performed on a large sample of random positions in the sky. We note that the above calculation does not take into account any cosmological evolution of the groups or the clusters where RGs lie; it is a pure effect of the SDSS selection of spectroscopic targets that decreases the number of cosmological neighbors when the redshift increases, as shown in our previous analysis (Massaro et al. 2019).

Finally, we also show in Figure 7 the number of optical galaxies with $m \leqslant m_{\rm src} + 2$, to highlight how the noise increases at higher redshift where the absolute magnitude of the central RG is fixed and apparent magnitude, $m_{\rm src}$, is rescaled.

5. Statistical Analyses

To provide additional evidence that both FR Is and FR IIs live in galaxy-rich large-scale environments, we performed the following statistical tests all based on the number of cosmological neighbors, $N_{\rm cn}$, surrounding them. It is worth noting that, as previously stated, the FRICAT used here is larger than the one adopted in our previous analysis since we also included the sFRICAT sample, allowing us to get a better sampling of the FR I population at lower redshifts.

The first test is based on the median of both FR I and FR II $N_{\rm cn}$ distributions. We computed median values of $N_{\rm cn}^{500}$ for FR Is (i.e., $\bar{N}_{\rm cn}^{500}$), per bin of $z_{\rm src}$ of size 0.01, and then we compared the distribution of $N_{\rm cn}^{500}$ for FR IIs with $\bar{N}_{\rm cn}^{500}$. We expect that if both RG populations live in large-scale environments of similar richness, 50% of the FR IIs would lie above the median value computed for the FR Is while 50% below, for each bin of $z_{\rm src}$. We also applied the same test to $N_{\rm cn}^{2000}$. All median values of both $N_{\rm cn}^{500}$ and $N_{\rm cn}^{2000}$ computed for the FR I population are reported in Table 1, together with the number of FR IIs that lie above and below the medians or have the same number of cosmological neighbors, per redshift bin.

For $N_{\rm cn}^{500}$, all 11 $z_{\rm src}$ bins have been explored, where we can compare FR Is and FR IIs. We found that in four cases the FR II median values are greater than $\bar{N}_{\rm cn}^{500}$ computed for FR Is, while in three cases the situation is the opposite, and in all of the remaining cases medians of the two populations show the same medians. This is in agreement with the expectations of a binomial distribution, thus strengthening our results that, independently of their radio morphology, both classes of FR Is and FR IIs live in similar galaxy-rich large-scale environments. The median values $\bar{N}_{\rm cn}^{500}$ for both populations of FR Is and FR IIs are shown in Figure 8. Then comparing $\bar{N}_{\rm cn}^{2000}$ the situation is in agreement with previous results with five cases for which $\bar{N}_{\rm cn}^{2000}$ of FR IIs is lower than that for the FR I population and five cases for which it is greater. Consequently, we can firmly confirm that the large-scale environments of the two classes of RGs, in each considered redshift range, are consistent.

Unfortunately, this first statistical test does not consider the two populations symmetrically, and it throws away almost all information about the distribution of environments present in the data. For example, if FR IIs have a systematically broader distribution of $N_{\rm cn}$ than FR Is, or a small tail of very rich, or very poor, environments, this first statistical test would be not sensitive to it. Thus, as a second statistical check, we also applied the Mann–Whitney U rank test (a.k.a. the Wilcoxon–Mann–Whitney test) to each redshift bin. In Figure 8 we also report, above each value of the medians of the two RG distributions of $N_{\rm cn}$ the normalized z_U variable, defined as $\frac{U - E(U)}{\sigma_U}$), computed for the Mann–Whitney U test and this is always consistent with zero, as expected, within the 2σ level of confidence, with the only exception of a single bin between

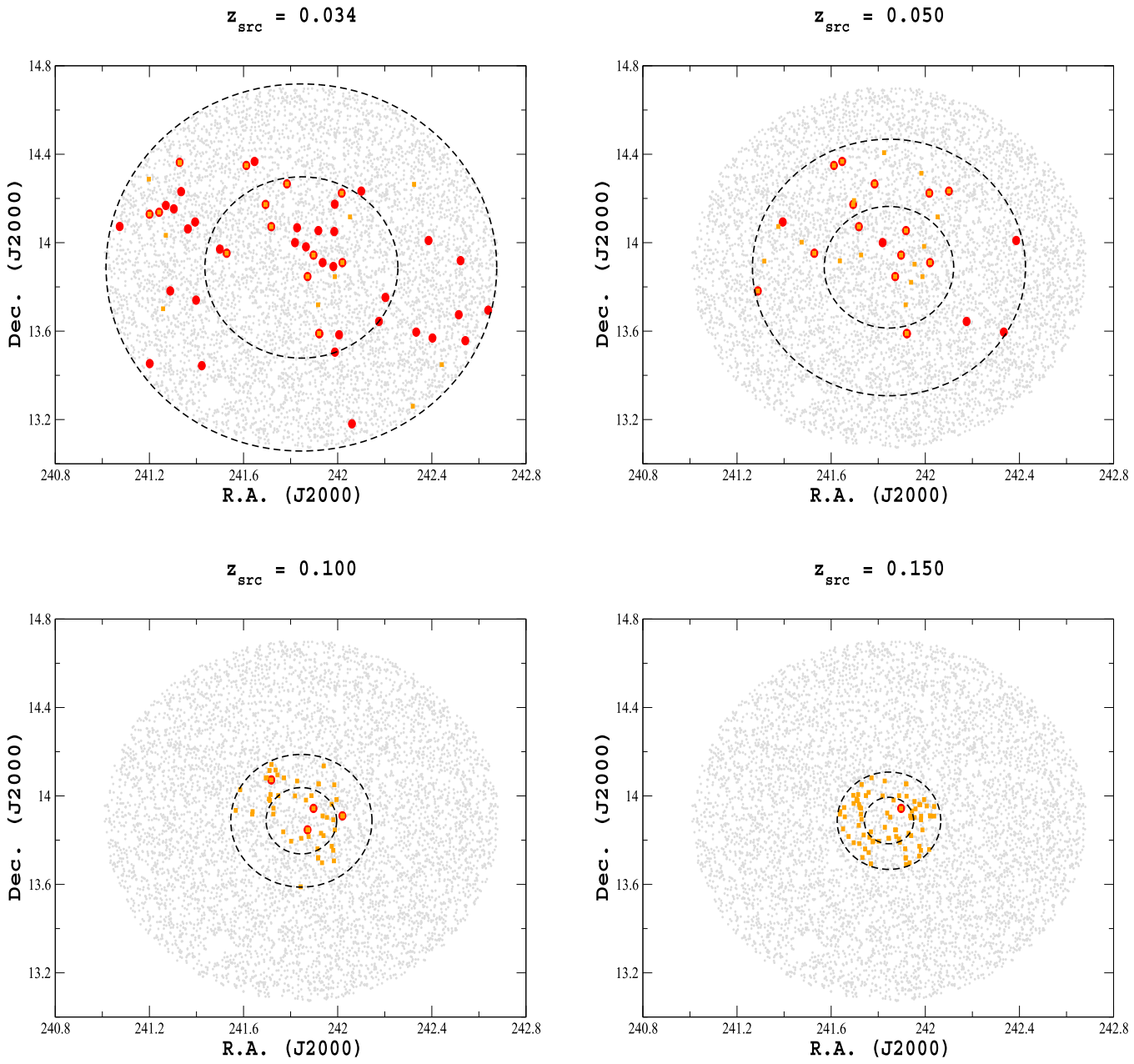

Figure 7. Spatial distributions of SDSS optical sources lying within 2 Mpc from the central RG at $z_{\rm src} = 0.034$ and having apparent magnitude in the R band greater than 19 are shown by the gray circles. Cosmological neighbors are highlighted with red circles. Orange squares mark the locations of optical galaxies with $m \leqslant m_{\rm src} + 2$, to highlight how the noise increases at higher redshift. Dashed black lines depict 1 Mpc and 2 Mpc distances from the central RG, respectively. In all other panels we show the distribution of cosmological neighbors computed assuming their intrinsic absolute magnitude, M_r, and rescaling their apparent magnitudes, m_r, at different redshifts, namely 0.05 (top right), 0.10 (bottom left), and 0.15 (bottom right), respectively. To create all plots at different redshifts than 0.034 we applied a cut for the rescaled apparent magnitude of the cosmological neighbors selecting only those brighter than 17.8. This limit corresponds to the SDSS criterion to select targets for spectroscopic observations. The number of cosmological neighbors decreases when their distances increase, while maintaining the intrinsic power of their host galaxies, strengthening our choice of having different thresholds at different redshifts to estimate cosmological overdensity.

$z = 0.13$ and $z = 0.14$ where the number $N_{\rm cn}$ for the FR IIs appears systematically lower than the median of FR Is (see Table 1). It is worth noting that we did not apply this test at $z < 0.08$ given the low number of FR IIs in these bins. Moreover, this second statistical test is also in agreement with our claim that the large-scale environments of FR Is and FR IIs cannot be distinguishable.

Then, for all redshift bins above 0.08 we also performed the two-sided Kolmogorov–Smirnov test between the distributions of $N_{\rm cn}^{500}$ and $N_{\rm cn}^{2000}$ of both FR Is and FR IIs. Results of the D variable computation as well as corresponding p-values are reported in Table 2, where the agreement with previous tests and the null hypothesis that the two distributions are the same cannot be rejected.

Finally, we verified the shape of the two $N_{\rm cn}$ distributions with a third statistical check computing the skewness and the Pearson median skewness and verifying that the signs of both these parameters correspond. This occurs in all redshift bins above 0.1 while below, the poor number of FR II radio galaxies in each z bin strongly affects both parameters, providing no significant results. Again this last test provides results in agreement with the previous ones.

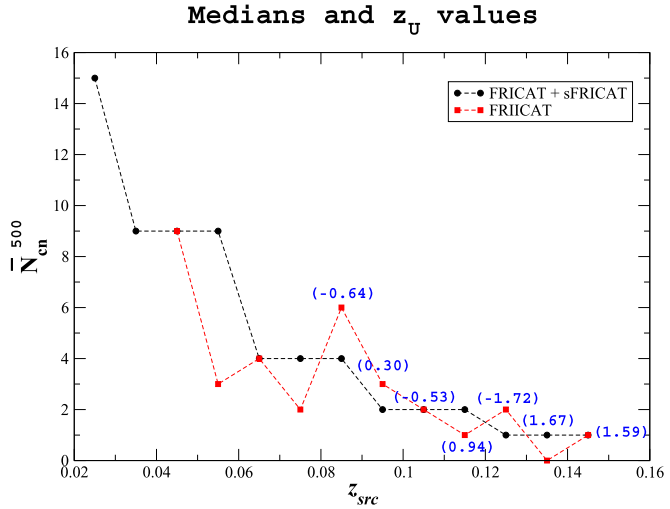

Figure 8. Median values for the FR I (black) and the FR II (red) RGs per bin of redshift $z_{\rm src}$. Together with the median measurements of FR Is we also report the number of FR IIs that lie above and below them in red and for each $z_{\rm src}$ bin. As shown these fractions of FR IIs are almost equally distributed around the medians of the FR I population as expected for sources inhabiting similar large-scale environments, independently of their radio extended structure. Blue numbers reported in parenthesis above each median value, at all redshift bins above 0.08, correspond to values computed for the z_U normalized variable of the Mann–Whitney U rank test (see Section 5 for more details).

Table 1
Comparison Between $\bar{N}^{500}_{\rm cn}$ and $\bar{N}^{2000}_{\rm cn}$ of FR Is with FR IIs

$z_{\rm src}$	$\bar{N}^{500}_{\rm cn}$	$N_{\rm FRII}$ > <=	$\bar{N}^{2000}_{\rm cn}$	$N_{\rm FRII}$ >< =
0.045	9	0–0–1	44	1–0–0
0.055	9	1–4–0	50	1–4–0
0.065	4	1–2–1	18	2–1–1
0.075	4	2–4–0	23	2–4–0
0.085	4	6–2–0	12	6–1–1
0.095	2	5–4–0	11	3–6–0
0.105	2	5–5–4	9	6–7–1
0.115	2	2–7–3	5	6–5–1
0.125	1	6–0–5	5	6–5–0
0.135	1	3–10–4	8	1–15-1
0.145	1	3–14–11	3	13–13–2
total	⋯	34–52–29	⋯	47–61–7

Note. Column (1) contains the central value of each redshift bin; columns (2) and (4) contain the median values for the $N^{500}_{\rm cn}$ and $N^{2000}_{\rm cn}$ parameters computed for the FR I population; columns (3) and (5) show the number of FR IIs (i.e., $N_{\rm FRII}$) lying above (>), below (<), and equal to (=) these median values.

6. Environmental Properties

6.1. Environmental Parameters: Definition

On the basis of the distribution of the cosmological neighbors it is possible to estimate several parameters to investigate the properties of the large-scale environments surrounding FR Is and FR IIs and compare them with those of the central RGs.

In particular, we defined the following quantities.

1. The concentration parameter, $\zeta_{\rm cn}$, is defined as the ratio of the number of cosmological neighbors lying within 500 kpc and those within 1 Mpc. This parameter allows us to test if the RG tends to lie close to the center of the group or clusters of galaxies around it or in its outskirt. A similar concentration parameter has been estimate using candidate elliptical galaxies rather than cosmological neighbors: $\zeta_{\rm el}$.
2. The average projected distance $d_m^{\rm cn}$ of the distribution of cosmological neighbors computed between their position and that of the central RG.
3. The standard deviation σ_z of the redshift distribution of the cosmological neighbors surrounding each RG.

All values for the environmental parameters described above are also reported in Table 3 in the Appendix.

Table 2
Results of the Two-sided Kolmogorov–Smirnov Test Run for the FR I and the FR II Distributions of $N^{500}_{\rm cn}$ and $N^{2000}_{\rm cn}$

$z_{\rm src}$	$D(N^{500}_{\rm cn})$	$p(N^{500}_{\rm cn})$	$D(N^{2000}_{\rm cn})$	$p(N^{2000}_{\rm cn})$
0.085	0.289	0.804	0.337	0.629
0.095	0.291	0.760	0.368	0.469
0.105	0.232	0.816	0.223	0.851
0.115	0.172	0.986	0.235	0.831
0.125	0.296	0.499	0.269	0.622
0.135	0.224	0.650	0.382	0.084
0.145	0.205	0.445	0.089	0.999

Note. Column (1) contains the central value of each redshift bin; columns (2) and (4) contain the D statistical variable; columns (3) and (5) contain the corresponding p-value for the distributions of $N^{500}_{\rm cn}$ and $N^{2000}_{\rm cn}$, respectively.

6.2. Environmental Parameters: Statistical Analysis

We investigated the distribution of the environmental parameters previously defined searching for possible trends in the RG properties, such as the absolute magnitude in the R band, M_r, the radio luminosity, L_R, and the [O III] emission line luminosity, $L_{\rm [O\ III]}$.

The distribution of the concentration parameter, $\zeta_{\rm cn}$, for both FRICAT and FRIICAT is shown in Figure 9. There are 52 FR Is out of 209 and 34 FR IIs out of 115 that have no cosmological neighbors within 500 kpc of their position. However, this does not imply that their large-scale environment is not rich since it could be due, for example, to the SDSS spectroscopic incompleteness and/or to the position of the RG in the outskirts of its galaxy-rich large-scale environment. Most of the remaining RGs indeed appear to inhabit an environment with high galaxy density.

We note that the distribution of sources around a random position in the sky follows, in general, a uniform distribution, where the number of sources is expected to scale as $N \propto \vartheta^2$, with ϑ being the angular separation from the random position. Thus assuming that the same situation could be applicable to cosmological neighbors, the expected value of the $\zeta_{\rm cn}$ is 0.25 while the largest fraction of the observed values is significantly higher.

In Figure 10 we show the comparison between the concentration indices of FR Is computed using the number of cosmological neighbors, $\zeta_{\rm cn}$, and that of candidate elliptical galaxies, $\zeta_{\rm el}$. The distribution of $\zeta_{\rm el}$ is peaking around 0.4 and has the largest fraction of values in the range 0.2–0.6. There are lower values around zero since it is "easier" to find candidate elliptical galaxies than cosmological neighbors due to the SDSS fiber cladding, which prevents fibers from being placed closer than 55″. A similar situation occurs for FR IIs.

We conclude that, independently of the concentration parameter adopted, RGs appear to inhabit galaxy-rich large-scale

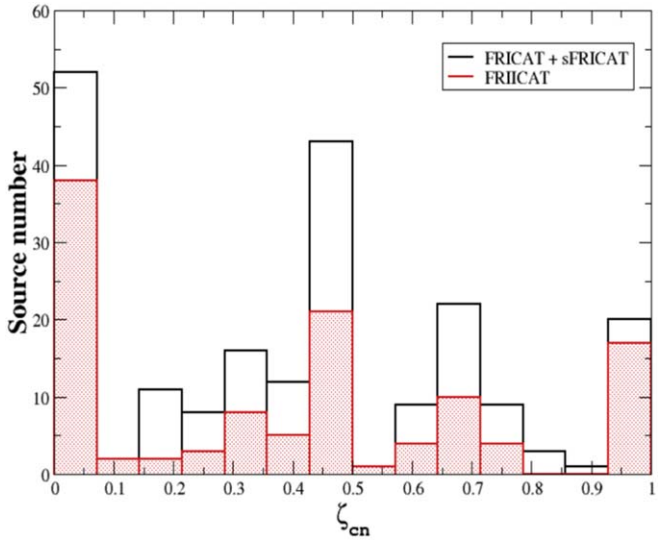

Figure 9. Distribution of the concentration parameter ζ_{cn} estimate using the distribution of the cosmological neighbors. Black histogram refers to the FR I population while the red one to the FR IIs. The two distributions for different RG classes are similar and the largest fraction of their values lie above the value of 0.25, which is expected assuming a uniform distribution of cosmological neighbors. Values of ζ_{cn} in the first bin (i.e., close to zero) are simply due to the lack of cosmological neighbors within 500 kpc distance from the central RG.

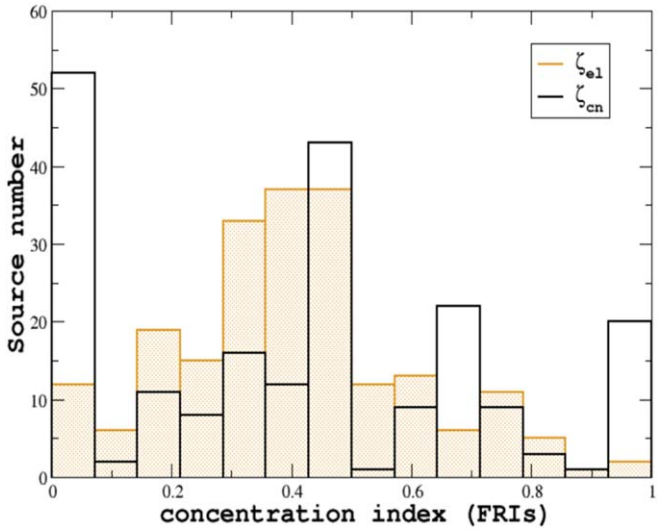

Figure 10. Comparison between the concentration indices computed using the number of cosmological neighbors ζ_{cn} (black) and that using candidate elliptical galaxies ζ_{el} (orange) for the FR I population. The main difference between the two distributions is the decreasing of the low values when using ζ_{el} with respect to ζ_{cn}. This is due to the fact that it is easier to find candidate elliptical galaxies with respect to cosmological neighbors. However, both parameters provide similar information.

environments lying closer to the centroid of both cosmological neighbors and candidate elliptical galaxies.

Moreover, in Figure 11 we also report the value of ζ_{cn} as a function of the source redshift z_{src}. We do not see any trend/correlation between these two parameters or differences between the two RG classes.

We explore the distribution of the average projected distance, d_m^{cn}, of the distribution of cosmological neighbors and the standard deviation, σ_z, of their redshift distribution. These parameters provide an estimate of the group/cluster

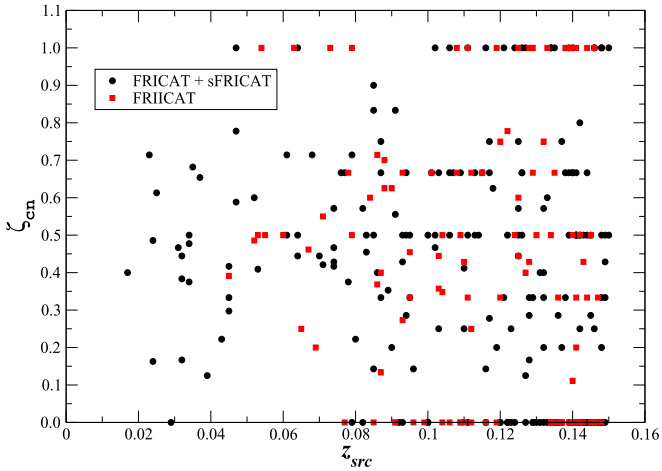

Figure 11. Concentration parameter, ζ_{cn}, as function of redshift, z_{src}, for both FR Is in black circles and FR II in red squares. No trend between these two parameters is evident; thus, we can claim that there is no cosmological evolution of the concentration parameter. Values of ζ_{cn} in the first bin (i.e., close to zero) are simply due to the lack of cosmological neighbors within 500 kpc of the central RG.

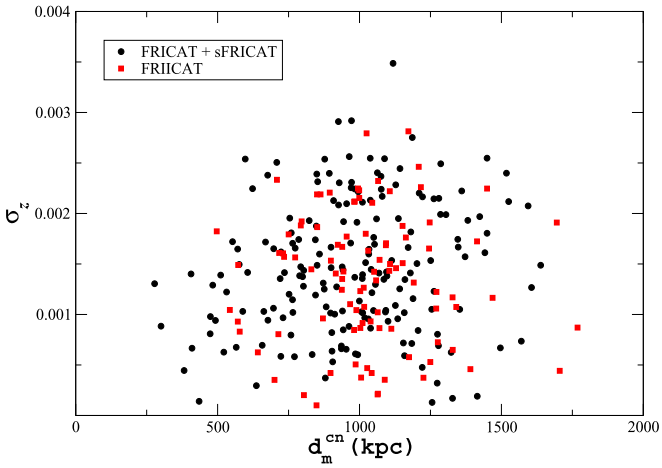

Figure 12. Comparison between the average projected distance, d_m^{cn}, of the distribution of cosmological neighbors and the standard deviation, σ_z, of their redshift distribution for both RG classes, namely, FR Is shown by black circles and FR IIs by red squares. No trend is evident between these two parameters.

physical size. Their comparison is shown in Figure 12. We did not find any trend between these two parameters for both classes of RGs, as shown by their distributions in Figure 13. In the latter case, we carried out a two-sided Kolmogorov–Smirnov test and we found the D parameter equal to 0.113 and corresponding to a p-value of 0.395 for a total number of 186 values of σ_z for the FR Is and 96 for the FR IIs, thus indicating that the null hypothesis that the two distributions are the same cannot be rejected. However, as shown in Figure 14, we found that for high values of N_{cn}^{2000} the redshift dispersion σ_z appears clustered around the 0.002.

In Figure 15 we also show the values of both parameters, d_m^{cn} and σ_z, as functions of z_{src} but no evidence of any trend is found.

Finally, we explored other links between parameters of the central RG and those of the surrounding environments but no neat trends are evident. Figures are shown in the Appendix.

We show d_m^{cn} and σ_z in comparison with the absolute magnitude in the R band of the RG where no trend/link is

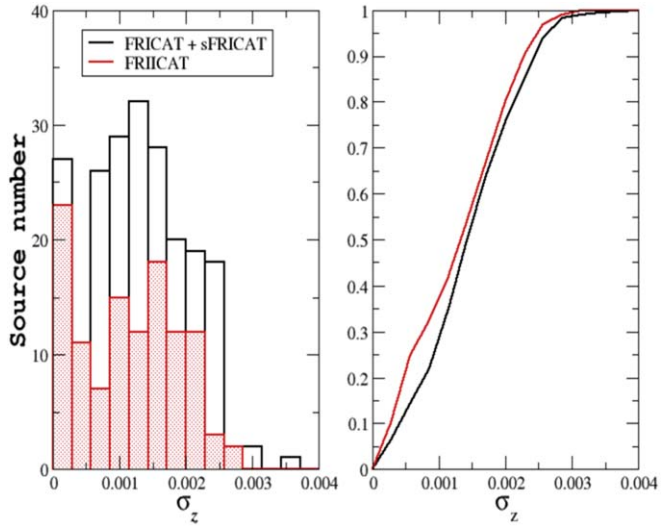

Figure 13. In the left panel, we show the histogram of the standard deviation, σ_z, for redshift distribution of cosmological neighbors lying within 2 Mpc. The black histogram shows the behavior of FR Is and the red one that of FR IIs. Cumulative distributions, drawn from the binned histograms, are also shown in the right panel.

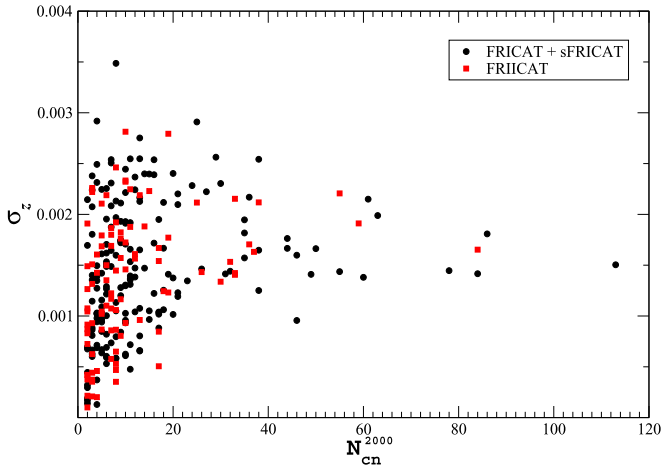

Figure 14. Comparison between the standard deviation σ_z of the redshift distribution of the cosmological neighbors and the number of cosmological neighbors within 2 Mpc: N_{cn}^{2000}, a parameter used to estimate the environmental richness. There is a trend between these two parameters, with environments with larger N_{cn}^{2000} appearing to have larger values of σ_z. Black circles indicate FR Is belonging to both the FRICAT and the sFRICAT while red squares mark FR IIs.

identified. A similar situation occurs also when comparing both of these environmental parameters with radio power, L_R, and emission line luminosity of the [O III], i.e., $L_{[O\ III]}$. The plot with $L_{[O\ III]}$ allows us to test if there are differences between LERGs and HERGs; however, these results must be treated with caution since the number of HERGs is quite low, thus making this comparison less statistically significant. We conclude that, independent of the power of the central RG in different energy ranges or that of its host galaxy, the properties of the large-scale environment for HERGs and LERGs is the same, being also independent by their radio morphology.

7. X-Ray Perspectives

We converted the standard deviation, σ_z, of the redshift distribution computed using all cosmological neighbors within 2 Mpc, N_{cn}^{2000}, into an estimate of the velocity dispersion, σ_v, of galaxies in the large-scale environments of radio galaxies. We computed the standard deviation of the line-of-sight component of the velocity (i.e., radial velocity) according to Danese et al. (1980), thus using the following relation:

$$v_{\parallel} = \frac{c(z_{src} - \langle z \rangle_{cn})}{1 + \langle z \rangle_{cn}}, \quad (1)$$

where z_{src} is the redshift of the central radio galaxy and $\bar{z}_{cn}$ is the average redshift of all cosmological neighbors within 2 Mpc. In Figure 16 we show the distribution of the velocity dispersion computed on the basis of Equation (1).

Then, considering σ_v, we also assumed that groups and clusters surrounding radio galaxies, being gravitationally bound, are virialized and thus we estimated the total mass M_{env}, i.e., galaxies plus IGM plus dark matter content, for their large-scale environments, according to

$$M_{env} = \frac{\sigma_v^2 R_{vir}}{3G}, \quad (2)$$

where we assumed $R_{vir} = 2$ Mpc and we neglect the form factor $3/5$.

We finally adopted two different correlations to estimate the X-ray luminosity L_X and the X-ray integrated flux F_X. The first correlation is

$$L_X = 3.3 \cdot 10^{26} \cdot M_{env}^{1.23}\ \mathrm{erg\ s^{-1}} \quad (3)$$

as reported by Reiprich & Böhringer (1999) while the second directly links σ_v with the X-ray luminosity:

$$\log\left(\frac{\sigma_v}{700\ \mathrm{km\ s^{-1}}}\right) = -0.003 + 0.346 \cdot \log\left(\frac{L_x\, E(z)^{-1}}{10^{44}\ \mathrm{erg\ s^{-1}}}\right) \quad (4)$$

found by Clerc et al. (2016), where $E(z) = [(1 + z_{src})^3 * \Omega_M + \Omega_\lambda]^{\frac{1}{2}}$.

Hence in Figure 17 we show the distribution of the environmental mass, M_{env}, as well as X-ray fluxes, F_X, estimated according to the previous relations and, using Equation (3), as expected, they are all below the threshold of 4.4×10^{-12} erg cm^{-1} s^{-1} of the *ROSAT* Brightest Cluster Sample (Ebeling et al. 1998). The same situation occurs for more than 95% of both radio galaxy catalogs when using Equation (4). We remark that both L_X estimates are also consistent with those derived using the L_X versus σ_v correlation found by Zhang et al. (2011).

X-ray detection of the IGM emission in the large-scale environments of these radio galaxies depends on several issues (e.g., distribution of the surface brightness, X-ray background, size of the galaxy cluster, etc.). However, assuming that the X-ray integrated flux is uniformly spread over a circular region of 500 kpc radius centered on the central radio source, the mean values of the X-ray intensity we estimated ranges between 3-4e−16 and 1e−14 for both FR Is and FR IIs, respectively; typical values of galaxy clusters are detected by satellites such as *XMM-Newton* and *Chandra* (see, e.g., Lloyd-Davies & Romer 2011; Mehrtens et al. 2012).

Finally, we selected two FR Is out of six radio galaxies for which X-ray observations are available in the *XMM-Newton* archive, and we carried out a simple analysis to show that low exposure times (∼5 ks) can guarantee the X-ray detection of

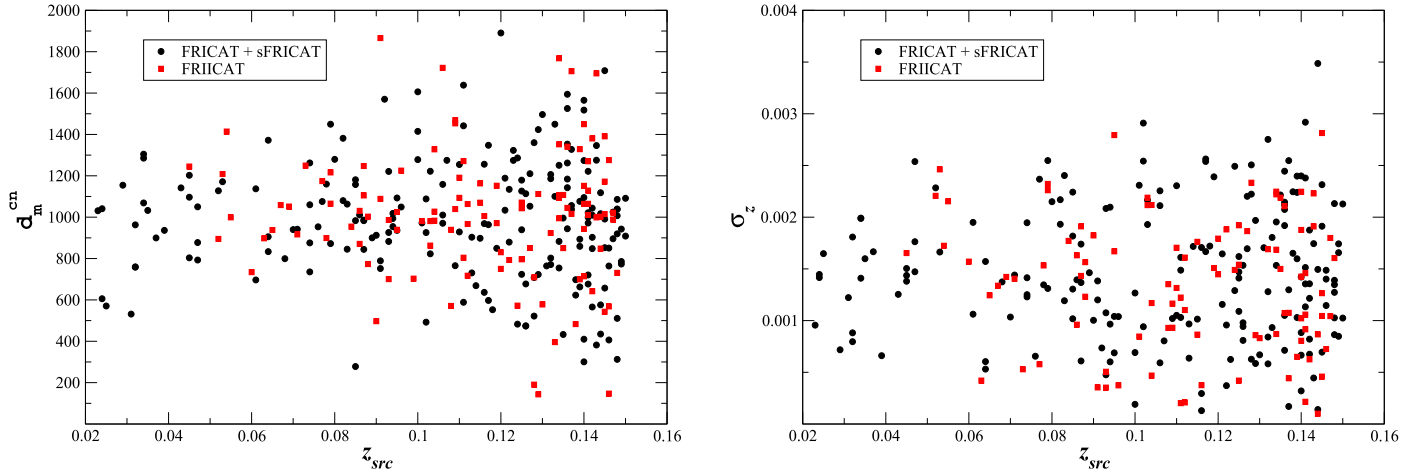

Figure 15. (Left panel) The average projected distance, d_m^{cn}, of the distribution of cosmological neighbors vs. the redshift, z_{src}, of the central RG. (Right panel) Same as the left panel for the σ_z parameter. FR Is are represented as black circles and FR IIs as red squares in both panels. No clear trend was found between these parameters and the RG redshift.

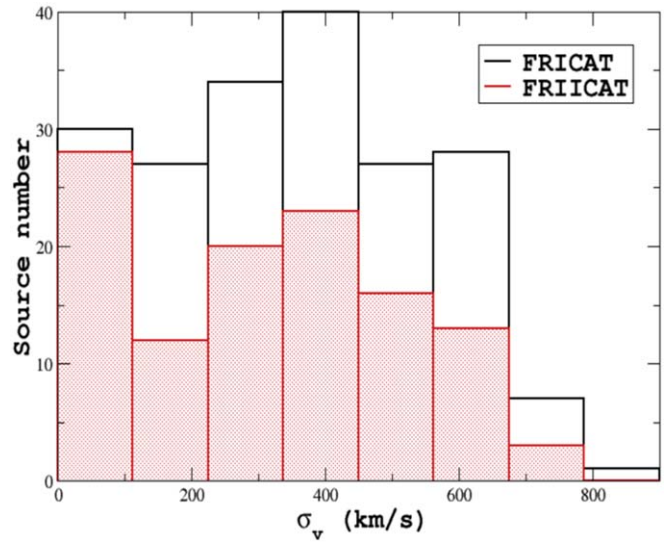

Figure 16. Distribution of the velocity dispersion for both FRICAT and FRIICAT sources derived according to Equation (1). As expected from their σ_z distribution, they are quite similar.

the IGM in the galaxy cluster around them as well as in the majority of the sources in explored catalogs. Selected sources are SDSS J113359.23+490343.4 and SDSS J120401.4 +201356.3, and we cut the exposure times of their archival data sets to 5.5 ks.

EPIC data were retrieved from the *XMM-Newton* Science Archive[10] and reduced with the SAS[11] 16.1.0 software. Following Nevalainen et al. (2005), we filtered XMM data for hard-band flares by excluding the time intervals where the high energy (9.5–12 keV for MOS1 and MOS1, 9.5–12 keV for PN) count rate evaluated on the whole detector FOV was more than 3σ away from its average value. To achieve a tighter filtering of background flares, we iteratively repeated this process two more times, re-evaluating the average hard-band count rate and excluding time intervals more than 3σ from this value. The same procedure was applied to soft 1–5 keV band restricting the analysis to an annulus with inner and outer radii of $12'$ and $14'$, where the emission from the radio galaxy is expected to be small.

We merged data from MOS1, MOS2, and PN detectors from all observations using the MERGE task, to detect the fainter sources that would not be detected otherwise. Sources were detected on these merged images following the standard SAS sliding box task EDETECT_CHAIN that mainly consists of three steps: (i) source detection with local background, with a minimum detection likelihood of 8; (ii) removal of sources in step 1 and creation of smooth background maps by fitting a 2D spline to the residual image; and (iii) source detection with the background map produced in step 2 with a minimum detection likelihood of 10.

The task EMLDETECT was then used to determine the parameters for each input source by means of a maximum likelihood fit to the input images, selecting sources with a minimum detection likelihood of 15 and a flux in the 0.3–10 keV band larger than 10^{-14} erg cm^{-2} s^{-1} (assuming an energy conversion factor of 1.2×10^{-11} cts cm^2 erg^{-1}). An analytical model of the point-spread function (PSF) was evaluated at the source position and normalized to the source brightness. The source extent was then evaluated as the radius at which the PSF level equals half of the local background. We finally visually inspected the detected sources and removed evident spurious detections (i.e., at chip borders, in regions of diffuse emission, etc.). We then produced "swiss-cheese" images for each detector array and observation.

As shown in the upper panels of Figure 18 we clearly detected extended X-ray emission in the merged *XMM-Newton* archival images around each radio galaxy, while in the lower panels of Figure 18 the surface brightness profiles are also reported.

It is also worth mentioning that we measured the integrated X-ray flux over a circular region of size equal to the maximum extent of the X-ray diffuse emission, evaluated by the surface brightness profiles, and it is in agreement with those values estimated using Equations (3) and (4) for all three radio galaxies.

8. Summary and Conclusions

We carried out an extensive investigation of the RG large-scale environment in the local universe (i.e., at $z_{src} \leqslant 0.15$).

[10] http://nxsa.esac.esa.int/nxsa-web
[11] http://www.cosmos.esa.int/web/XMM-Newton/sas

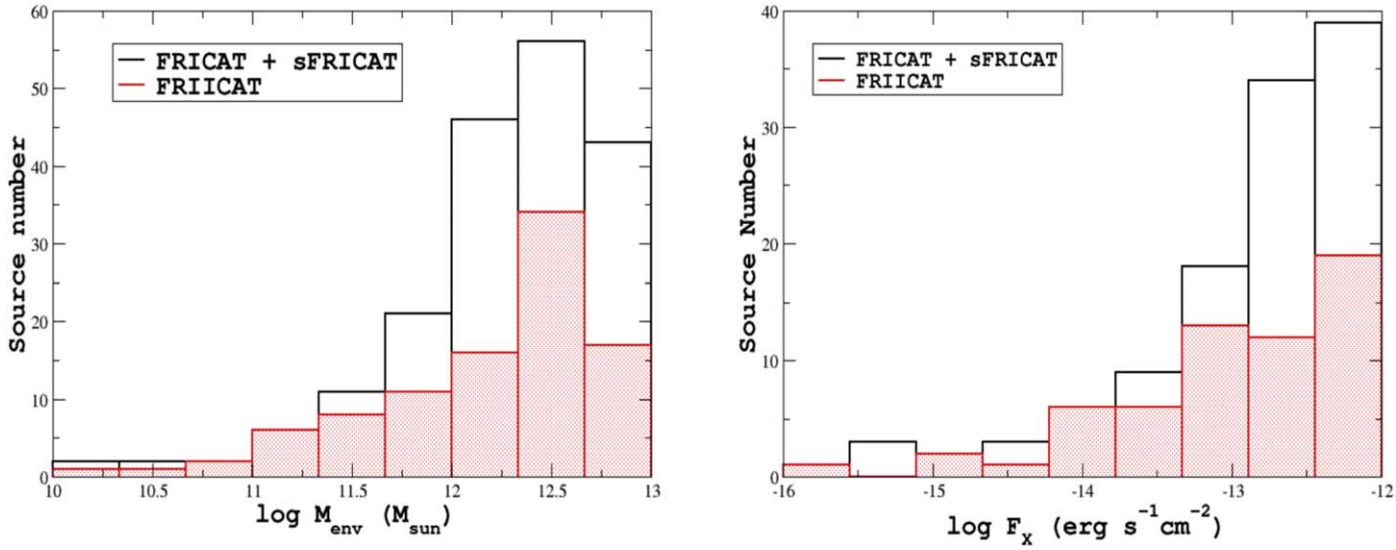

Figure 17. (Left panel) The distribution of the environmental mass derived from the virial theorem. (Right panel) The distribution of the integrated X-ray fluxes estimated from the velocity dispersion and the correlation of Equation (3).

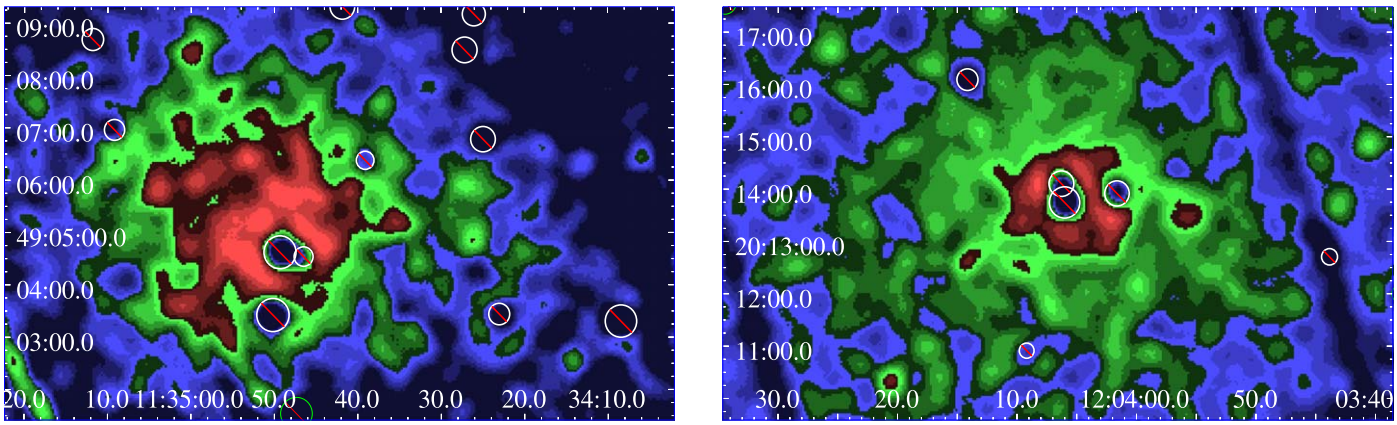

Figure 18. "Swiss-cheese" images for two FR Is with *XMM-Newton* archival observations cut to 5.5 ks exposure time, namely SDSS J113359.23+490343.4 (left panel) and SDSS J120401.4+201356.3 (right panel). These images show the clear detection of extended X-ray emission around both FR Is using merged *XMM-Newton* observations. Images are background and point-source subtracted and normalized for the exposure map. Then we also smoothed them with a Gaussian kernel of 8 pixels. White circular regions mark the location of all point sources detected during our data reduction procedure lying in the field.

Our analysis was based on the comparison of different clustering algorithms and on the development of a new method, based on the counts of cosmological neighbors: optical sources lying within 2 Mpc and with a redshift difference $\Delta z \leqslant 0.005$ with respect to the RG lying at the center of the field examined, a method known as cosmological overdensity. Our study was also based on extremely homogeneous RG catalogs, with uniform radio, infrared, and optical data available for all sources, allowing us to distinguish between FR I and FR II or LERG versus HERG. We found that independently of their radio morphological classification they all appear to live in similar galaxy-rich large-scale environments. The same result, even if less statistically significant, was also obtained while investigating LERG versus HERG environments (M19).

Here we first performed a dedicated analysis to show how cosmological biases and artifacts can affect analyses of RG large-scale environments and how the cosmological overdensity is almost not affected. Then, even if our procedure is dependent on the SDSS selection of spectroscopic targets, it permits us to obtain better estimates of (i) the ambient richness, (ii) the center of the galaxy distribution surrounding target RGs, and (iii) the redshift difference between central RG and the average values of cosmological neighbors, which seems to be a better estimate of the environmental redshift. We stress the importance of comparing radio sources in the same redshift bins to obtain a complete overview of their large-scale environments, in particular, for procedures not based on spectroscopic redshift estimates.

We also presented an additional statistical test based on the distribution of the median values of the RG population that showed, consistently with our previous analysis, how FR Is and FR IIs live in large-scale environments having environments that are indistinguishable on the basis of the statistical analysis we carried out, at all redshifts up to $z_{\rm src} = 0.15$. The lack of a significant number of HERGs (only 14 out of 105 total RGs) listed in the FRIICAT prevents us from drawing firm conclusions on the comparison between them and LERGs and thus it was not explored.

In the current paper we also investigated several properties of the RG environments on megaparsec scale using the

cosmological neighbors distribution and a few parameters derived. Our main results are summarized as follows.

1. The concentration parameter, $\zeta_{\rm cn}$, defined as the ratio between the number of cosmological neighbors within 500 kpc and those within 1 Mpc, does not depend by the RG redshift, $z_{\rm src}$, and has a distribution that does not depend by the radio classification (i.e., FR I versus FR II). Typical values of $\zeta_{\rm cn}$ are well above 0.25 expected by a uniform distribution of surrounding cosmological neighbors. Consistent results are obtained even when using the number of candidate elliptical galaxies instead of the cosmological neighbors.
2. FR Is and FR IIs also have similar distributions of the standard deviation, σ_z, of the redshift distribution of the cosmological neighbors as well as their average projected distance, $d_m^{\rm cn}$, computed between their position and that of the central RG. This implies that in the redshift range explored the RG environments have similar sizes.
3. When comparing the properties of the cosmological neighbors with those of the central RGs, as the absolute magnitude, M_r, the radio power, L_R, and [O III] emission line luminosity, we did not find any trend or any difference between FR I and FR II populations.

Finally, we used the σ_z parameter to estimate the velocity dispersion of cosmological neighbors and assumed that this is the same for all galaxies belonging to the large-scale environment of both RG populations. Then under the assumption that these RG environments are virialized we estimated the total mass, $M_{\rm env}$, present therein, i.e., mass of galaxies plus IGM plus dark matter content.

Thanks to the correlations between $M_{\rm env}$ and the X-ray luminosity, $L_{\rm X}$, of the IGM we also computed the expected values necessary to draw the feasibility of future X-ray campaigns and/or pave the path to what eROSITA will be able to detect in the near future. Given the same distribution of σ_z and the lack of any trend with this parameter with those of the central radio galaxies (i.e., M_r, L_R, and $L_{\rm [O\ III]}$) the same situation occurs with the derived quantities: $M_{\rm env}$ and $L_{\rm X}$ of their large-scale environments. However, the estimates of X-ray fluxes confirm that X-ray counterparts of the groups and clusters of galaxies around FRICAT and FRIICAT sources should not be detected in the *ROSAT* all sky survey, demanding that *XMM-Newton* and *Chandra* facilities obtain a complete view of their large-scale environments. Finally, we reduced and analyzed *XMM-Newton* observations of two FR I radio galaxies, cutting the total exposure time to 5.5 ks, to show that a clear detection of galaxy clusters around them can be easily achieved with snapshot observations.

We thank the anonymous referee for useful and valuable comments that led to improvements in the paper, particularly, all of the statistical notes that were implemented in the revised version of the manuscript. F.M. wishes to thank Dr. C. C. Cheung for valuable discussions on this project initially planned during the IAU 313 on the Galapagos islands. This work is supported by the "Departments of Excellence 2018–2022" Grant awarded by the Italian Ministry of Education, University and Research (MIUR) (L. 232/2016). This research has made use of resources provided by the Compagnia di San Paolo for the grant awarded on the BLENV project (S1618_L1_MASF_01) and by the Ministry of Education, Universities and Research for the grant MASF_FFABR_17_01. This investigation is supported by the National Aeronautics and Space Administration (NASA) grants GO6-17081X and GO9-20083X. F.M. acknowledges financial contribution from the agreement ASI-INAF n.2017-14-H.0. Funding for SDSS and SDSS-II has been provided by the Alfred P. Sloan Foundation, the Participating Institutions, the National Science Foundation, the U.S. Department of Energy, the National Aeronautics and Space Administration, the Japanese Monbukagakusho, the Max Planck Society, and the Higher Education Funding Council for England. The SDSS website is ; http://www.sdss.org/. The SDSS is managed by the Astrophysical Research Consortium for the Participating Institutions. The Participating Institutions are the American Museum of Natural History, Astrophysical Institute Potsdam, University of Basel, University of Cam- bridge, Case Western Reserve University, University of Chicago, Drexel University, Fermilab, the Institute for Advanced Study, the Japan Participation Group, Johns Hopkins University, the Joint Institute for Nuclear Astrophysics, the Kavli Institute for Particle Astrophysics and Cosmology, the Korean Scientist Group, the Chinese Academy of Sciences (LAMOST), Los Alamos National Laboratory, the Max- Planck-Institute for Astronomy (MPIA), the Max-Planck-Institute for Astrophysics (MPA), New Mexico State University, Ohio State University, University of Pittsburgh, University of Portsmouth, Princeton University, the United States Naval Observatory, and the University of Washington. TOPCAT and STILTS astronomical software (Taylor 2005) were used for the preparation and manipulation of the tabular data and the images.

Appendix
Figures and Tables

Figures 19–21 show the behavior of the environmental parameters: $d_m^{\rm cn}$ and σ_z as functions of M_R, L_R, and $L_{\rm [O\ III]}$, respectively. However, no trends were found in these cases. Then, in Table 3, we report all ambient parameters estimated for each RG analyzed.

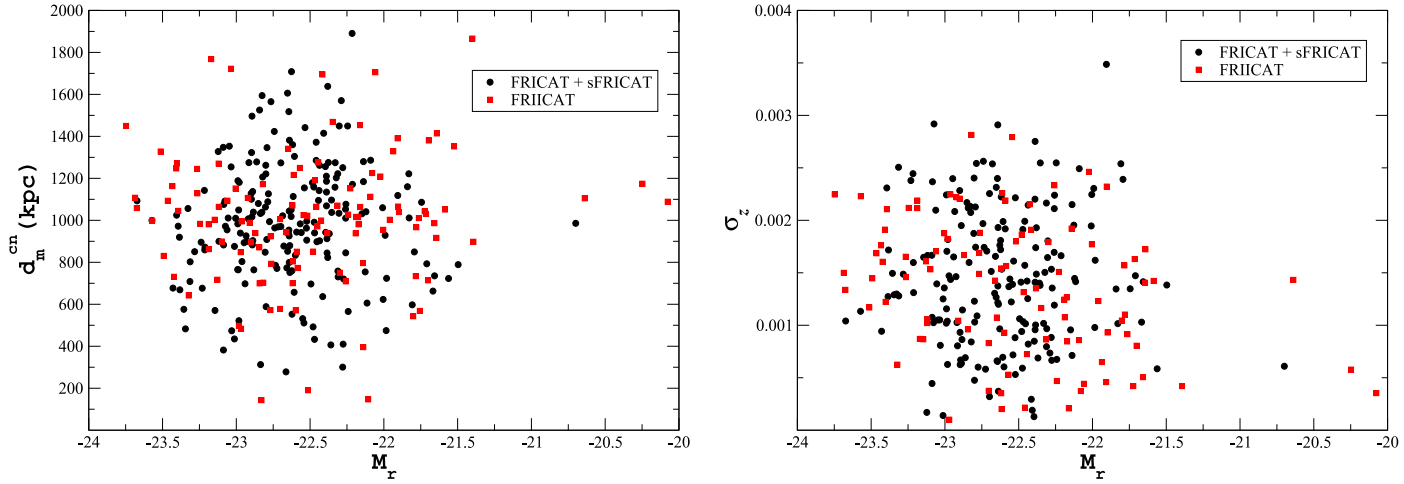

Figure 19. (Left panel) The scatter plot of the average projected distance, $d_m^{\rm cn}$, of the distribution of cosmological neighbors as a function of the absolute magnitude, M_r, of the central radio galaxy for both FR Is (black circles) and FR IIs (red squares). No neat trend or correlation is found between these two parameters. (Right panel) The standard deviation, σ_z, of redshift distribution estimated using all cosmological neighbors lying within 2 Mpc as a function of M_r of the central RG. Again FR Is are marked as black circles while FR IIs as red squares.

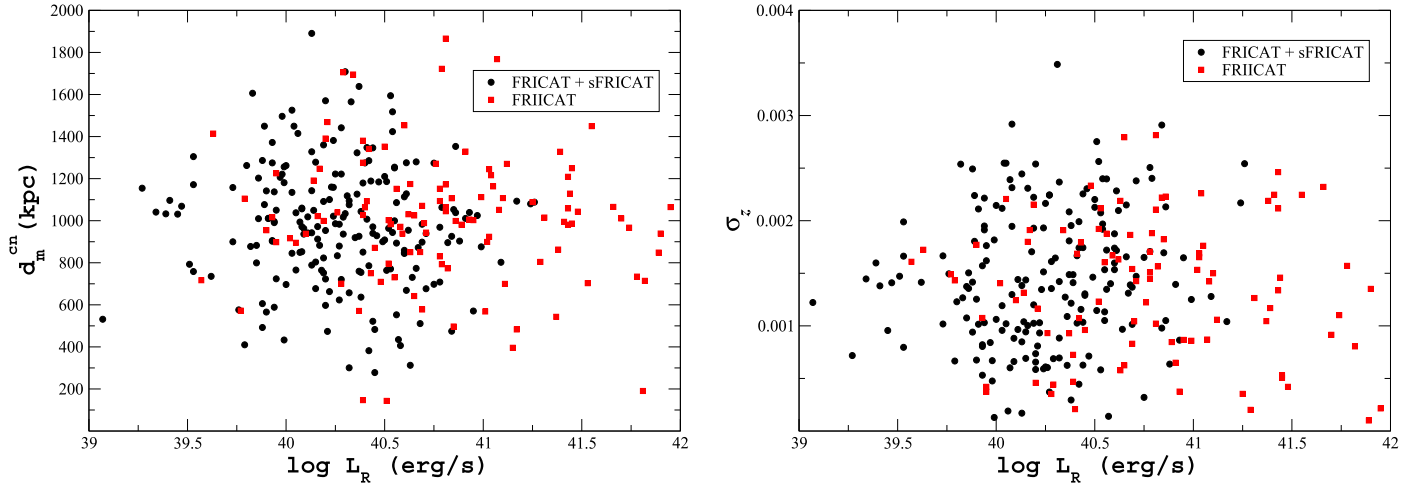

Figure 20. Same as the left panel and the right panel of Figure 19 but as a function of the radio luminosity, respectively.

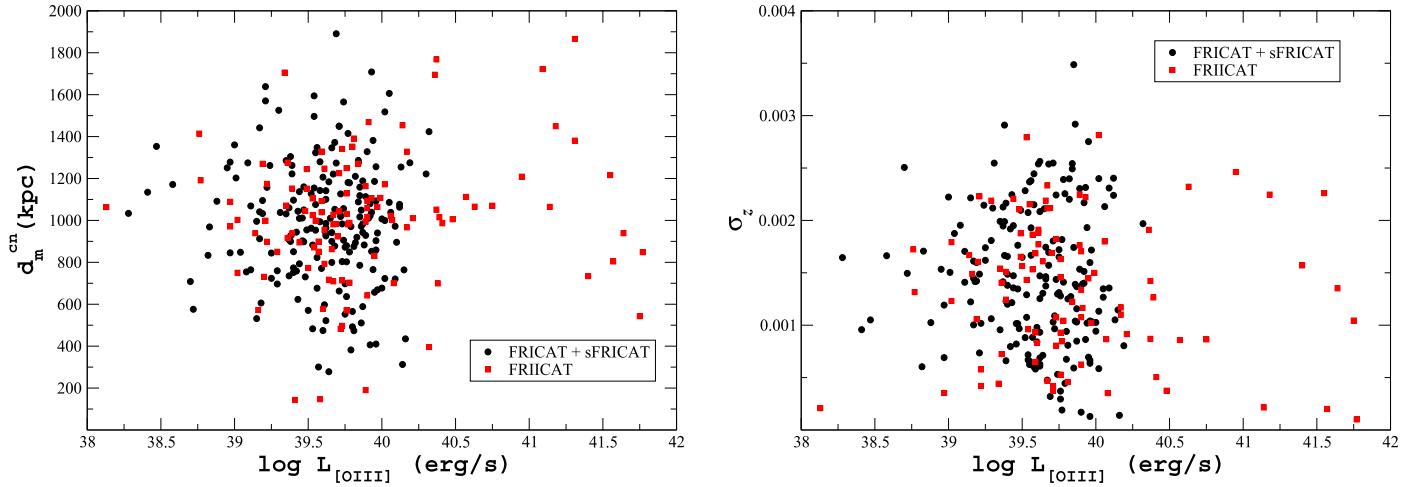

Figure 21. Same as the left panel and the right panel of both Figures 19 and 20 but as a function of the [O III] emission line luminosity, respectively.

Table 3
Environmental Parameters for the FRICAT and the FRIICAT (First 10 Lines)

SDSS Name	Radio Class	z_{src}	Δz	d_{proj} (kpc)	N_{cn}^{500}	N_{cn}^{1000}	N_{cn}^{2000}	ζ_{cn}	$\langle z_{cn} \rangle$	σ_z	d_{proj}^{cn} (kpc)	d_m^{cn} (kpc)	σ_v (km s^{-1})	M_{env} ($M_\odot$)	F_X (erg cm^{-2} s^{-1})
J073014.37+393200.4	FRI	0.142	5.3E−4	450.42	1	4	6	0.25	0.141	0.00082	207.56	902.48	215.61	11.86	−13.18
J073505.25+415827.5	FRI	0.087	5.2E−4	161.92	3	4	10	0.75	0.088	0.00061	758.00	985.60	168.04	11.64	−13.05
J073719.18+292932.0	FRI	0.111	8.1E−4	159.92	1	1	5	1.00	0.108	0.00161	826.91	1441.76	436.15	12.47	−12.07
J074125.85+480914.3	FRI	0.12	⋯	⋯	0	0	1	⋯	0.115	⋯	1890.54	1890.55	⋯	⋯	⋯
J074351.25+282128.0	FRI	0.106	3.0E−4	63.64	4	4	9	1.00	0.106	0.00211	258.80	1010.41	572.42	12.71	−11.69
J075221.83+333348.9	FRII	0.14	1.7E−4	111.63	2	2	4	1.00	0.138	0.00143	140.75	943.39	375.43	12.34	−12.47
J075309.91+355557.1	FRI	0.113	4.5E−4	180.50	2	4	5	0.50	0.113	0.00097	229.58	730.53	260.57	12.02	−12.73
J075506.67+262115.9	FRI	0.123	⋯	⋯	0	0	1	⋯	0.123	⋯	1274.66	1274.66	⋯	⋯	⋯
J075529.95+520450.6	FRII	0.14	⋯	⋯	0	0	0	⋯	⋯	⋯	⋯	⋯	⋯	⋯	⋯
J075628.78+501716.3	FRII	0.134	⋯	⋯	0	0	2	⋯	0.133	0.00087	322.70	1768.24	230.16	11.91	−13.04

Note. Column (1): SDSS name. Column (2): radio class to distinguish between sources belonging to the FRICAT and the FRIICAT. Column (3): source redshift. Column (4): absolute value of the redshift difference between the RG and the closest galaxy cluster in the T12 catalog. Column (5): physical distance between the RG and the closest galaxy cluster in the T12 catalog. This is computed at the z_{src} of the central RG. Columns (6, 7, 8): number of cosmological neighbors within 500, 1000, and 2000 kpc, respectively, estimated at the z_{src} of the central radio galaxy. Column (9): the concentration parameter ζ_{cn}. Column (10): the average redshift of the cosmological neighbors in 2 Mpc. Column (11): the standard deviation of the redshift distribution for the cosmological neighbors within 2 Mpc. Column (12): physical distance between the central RG and the average position of the cosmological neighbors within 2 Mpc. This is computed at the z_{src} of the central RG. Column (13): average distance of the cosmological neighbors within 2 Mpc. Column (14): velocity dispersion of the cosmological neighbors located in 2 Mpc. Column (15): environmental mass estimated from the velocity dispersion. Column (16): X-ray flux estimated from the velocity dispersion.

(This table is available in its entirety in machine-readable form.)

ORCID iDs

F. Massaro https://orcid.org/0000-0002-1704-9850
A. Capetti https://orcid.org/0000-0003-3684-4275
A. Paggi https://orcid.org/0000-0002-5646-2410
R. D. Baldi https://orcid.org/0000-0002-1824-0411
I. Pillitteri https://orcid.org/0000-0003-4948-6550
R. Campana https://orcid.org/0000-0002-4794-5453

References

Abell, G. O., Corwin, H. G., Jr., & Olowin, O. P. 1989, ApJS, 70, 1
Ahn, C. P., Alexandroff, R., Allende Prieto, C., et al. 2012, ApJS, 203, 21
Baldi, R. D., Capetti, A., & Giovannini, G. 2015, A&A, 576A, 38
Baldi, R. D., Capetti, A., & Massaro, F. 2018, A&A, 609A, 1
Belsole, E., Worrall, D. M., Hardcastle, M. J., & Croston, J. H. 2007, MNRAS, 381, 1109
Bennett, C. L., Larson, D., Weiland, J. L., & Hinshaw, G. 2014, ApJ, 794, 135
Berlind, A. A., Frieman, J., Weinberg, D., et al. 2006, ApJS, 167, 1
Best, P. N. 2004, MNRAS, 351, 70
Best, P. N., & Heckman, T. M. 2012, MNRAS, 421, 1569
Biviano, A. 2000, in Proc. IAP Meeting, Constructing the Universe with Clusters of Galaxies, ed. F. Durret & D. Gerbal (Paris: IAP), 1
Blanton, E. L., Gregg, M. D., Helfand, D. J., Becker, R. H., & Leighly, K. M. 2001, AJ, 121, 2915
Blanton, E. L., Gregg, M. D., Helfand, D. J., Becker, R. H., & White, R. L. 2000, ApJ, 531, 118
Capetti, A., Massaro, F., & Baldi, R. D. 2017a, A&A, 598A, 49
Capetti, A., Massaro, F., & Baldi, R. D. 2017b, A&A, 601A, 81
Ching, J. H. Y., Croom, S. M., Sadler, E. M., et al. 2017, MNRAS, 469, 4584
Clerc, N., Merloni, A., Zhang, Y.-Y., et al. 2016, MNRAS, 463, 4490
Condon, J. J., Cotton, W. D., Greisen, E. W., et al. 1998, AJ, 115, 1693
Croston, J. H., Hardcastle, M. J., Birkinshaw, M., Worrall, D. M., & Laing, R. A. 2008, MNRAS, 386, 1709
D'Abrusco, R., Longo, G., & Walton, N. A. 2009, MNRAS, 396, 223
D'Agostini, G. 2003, Bayesian Reasoning in Data Analysis: A Critical Introduction (Singapore: World Scientific)
Danese, L., de Zotti, G., & di Tullio, G. 1980, A&A, 82, 322
Ebeling, H., Edge, A. C., Bohringer, H., et al. 1998, MNRAS, 301, 881
Eke, V. R. 2004, MNRAS, 348, 866
Evans, D. A., Worrall, D. M., Hardcastle, M. J., Kraft, R. P., & Birkinshaw, M. 2006, ApJ, 642, 96
Fadda, D., Girardi, M., Giuricin, G., Mardirossian, F., & Mezzetti, M. 1996, ApJ, 473, 670
Fanaroff, B. L., & Riley, J. M. 1974, MNRAS, 167, 31
Gendre, M. A., Best, P. N., Wall, J. V., & Ker, L. M. 2013, MNRAS, 430, 3086
Girardi, M., Biviano, A., Giuricin, G., Mardirossian, F., & Mezzetti, M. 1993, ApJ, 404, 38
Gladders, M. D., Lopez-Cruz, O., Yee, H. K. C., & Kodama, T. 1998, ApJ, 501, 571
Gladders, M. D., & Yee, H. K. C. 2000, ApJ, 120, 2148
Haas, M. R., Schaye, J., & Jeeson-Daniel, A. 2012, MNRAS, 419, 2133
Hardcastle, M. J., & Worrall, D. M. 2000, MNRAS, 319, 562
Helfand, D. J., White, R. L., & Becker, R. H. 2015, ApJ, 801, 26
Hill, G. J., & Lilly, S. J. 1991, ApJ, 367, 1
Hine, R. G., & Longair, M. S. 1979, MNRAS, 188, 111
Huchra, J. P., & Geller, M. J. 1982, ApJ, 257, 423
Ineson, J., Croston, J. H., Hardcastle, M. J., et al. 2013, ApJ, 770, 136
Ineson, J., Croston, J. H., Hardcastle, M. J., et al. 2015, MNRAS, 453, 2682
Laing, R. A., Jenkins, C. R., Wall, J. V., & Unger, S. W. 1994, in ASP Conf. Ser. 54, The First Stromlo Symp.: The Physics of Active Galaxies, ed. G. V. Bicknell, M. A. Dopita, & P. J. Quinn (San Francisco, CA: ASP), 201
Lintott, C. J., Schawinski, K., Slosar, A., et al. 2008, MNRAS, 389, 1179
Lloyd-Davies, E. J., Romer, A. K., Mehrtens, N., Hosmer, M., & Davidson, M. 2011, MNRAS, 418, 14
Massaro, F., Álvarez-Crespo, N., Capetti, N., et al. 2019, ApJS, 240, 20
Massaro, F., D'Abrusco, R., Ajello, M., et al. 2011, ApJ, 740L, 48
Massaro, F., D'Abrusco, R., Paggi, A., et al. 2013, ApJS, 209, 10
Massaro, F., Harris, D. E., Liuzzo, E., et al. 2015, ApJS, 220, 5
Massaro, F., Missaglia, V., Stuardi, C., et al. 2018, ApJS, 234, 7
Massaro, F., Tremblay, G. R., Harris, D. E., et al. 2012, ApJS, 203, 31
Mehrtens, N., Romer, A. K., Hilton, M., et al. 2012, MNRAS, 423, 1024
Mingo, B., Hardcastle, M. J., Croston, J. H., et al. 2014, MNRAS, 440, 269
Mingo, B., Hardcastle, M. J., Ineson, J., et al. 2017, MNRAS, 470, 2762
Miraghaei, H., & Best, P. N. 2017, MNRAS, 466, 4346
Moore, B., Frenk, C. S., & White, S. D. M. 1993, MNRAS, 261, 827
Nevalainen, J., Markevitch, M., & Lumb, D. 2005, ApJ, 629, 172
Prestage, R. M., & Peacock, J. A. 1988, MNRAS, 230, 131
Reiprich, T. H., & Böhringer, H. 1999, AN, 320, 296
Richards, G. T., Nichol, R. C., Gray, A. G., et al. 2004, ApJS, 155, 257
Rines, K., Geller, M. J., Diaferio, A., & Kurtz, M. J. 2013, ApJ, 767, 15
Sabater, J., Best, P. N., & Argudo-Fernàndez, M. 2013, MNRAS, 430, 638
Stuardi, C., Missaglia, V., Massaro, F., et al. 2018, ApJS, 235, 32
Tago, E., Saar, E., Tempel, E., et al. 2010, A&A, 514A, 102
Tasse, C., Best, P. N., Röttgering, H., & Le Borgne, D. 2008, A&A, 490, 893
Taylor, M. B. 2005, in ASP Conf. Ser. 347, Astronomical Data Analysis Software and Systems XIV, ed. P. Shopbell, M. Britton, & R. Ebert (San Francisco, CA: ASP), 29
Tempel, E., Tago, E., & Liivamägi, L. J. 2012, A&A, 540A, 106
Visvanathan, N., & Sandage, A. 1977, ApJ, 216, 214
White, R. L., Becker, R. H., Helfand, D. J., & Gregg, M. D. 1997, ApJ, 475, 479
Wilkes, B. J., Kuraszkiewicz, J., Haas, M., et al. 2013, ApJ, 773, 15
Wing, J. D., & Blanton, E. L. 2011, AJ, 141, 88
Worpel, H., Brown, M. J. I., Jones, D. H., Floyd, D. J. E., & Beutler, F. 2013, ApJ, 772, 64
Worrall, D. M., & Birkinshaw, M. 2000, ApJ, 530, 719
Wright, E. L., Eisenhardt, P. R. M., Mainzer, A. K., et al. 2010, AJ, 140, 1868
Zhang, Y. Y., Andernach, H., Caretta, C. A., et al. 2011, A&A, 526, A105
Zirbel, E. L. 1997, ApJ, 476, 489